Title: Desmoplakin is a desmosomal mechanosensor

Authors: Yinchen Dong [1], Ahmed Elgerbi [3], Bin Xie [2], John S. Choy [3], Sanjeevi Sivasankar [1, 2, *]

Affiliations: [1] Department of Biomedical Engineering, University of California, Davis, CA; [2] Biophysics Graduate Group, University of California, Davis, CA; [3] Department of Biology, The Catholic University of America, Washington DC.

***Corresponding author:** ssivasankar@ucdavis.edu

Abstract: Desmosomes are essential cell-cell adhesion organelles that enable tension-prone tissue, like the skin and heart, withstand mechanical stress. Desmosomal anomalies are associated with numerous epidermal disorders and cardiomyopathies. Despite their critical role in maintaining tissue resilience, an understanding of how desmosomes respond to mechanical stimuli is lacking. Here we demonstrate, in human breast cancer MCF7 cells, that actomyosin forces induce a conformational change in the N-terminal region of desmoplakin, a critical cytoplasmic desmosomal protein. Using super-resolution fluorescence microscopy, biochemical assays, and atomistic computer simulations, we show that actomyosin forces are directed to desmoplakin along keratin-19 filaments. These forces induce a conformational change in the N-terminal plakin domain of desmoplakin, converting this domain from a folded (closed) to an extended (open) conformation. Functional adhesion assays show that MCF7 cells with desmoplakin in an open conformation are more adhesive than cells with desmoplakin in a closed state. Our findings establish that desmoplakin is mechanosensitive and undergoes force-induced conformational changes which enhance the mechanical resilience of desmosomes.

Significance Statement: Desmosomes are essential cell-cell adhesion junctions that enable tension-prone tissue, like the skin and heart, withstand mechanical stress. Despite their critical role in maintaining tissue integrity, it is unclear how desmosomes respond to mechanical forces. Here we demonstrate that force induces a conformational change in desmoplakin, a critical intracellular desmosomal protein. This force-induced change in the desmoplakin's structure enhances the resilience of desmosomes and enables them to withstand mechanical stress.

Introduction

Desmosomes are critical cell-cell junctions that promote adhesion between cells and preserve tissue integrity. They are crucial in enabling tension-prone tissues like the skin and heart to withstand mechanical stresses [1]. Desmosomal anomalies are associated with numerous diseases in these tissues, such as epidermal autoimmune disorders and arrhythmogenic ventricular cardiomyopathy [2-4]. Despite their critical role in maintaining tissue mechanical resilience, an understanding of how desmosomes respond to mechanical stimuli is lacking.

Desmosomes are composed of transmembrane desmosomal cadherins: desmoglein (Dsg) and desmocollin (Dsc), and cytoplasmic plaque proteins: plakophilin, plakoglobin, and desmoplakin (DP). The extracellular regions of the cadherins from opposing cells interact to mediate adhesion while the plaque proteins bind to the cadherin cytoplasmic tail (Fig. 1A) [5]. DP anchors desmosomes to the keratin intermediate filament (KIF) cytoskeleton, and this linkage is essential for maintaining tissue integrity and facilitating intracellular signal transduction [6, 7]. Several studies show that KIFs work in cooperation with the actomyosin cytoskeleton to modulate the mechanical state of desmosomes [8-10]. Disassociation of KIFs from circumferential actin belts alters tension across desmosomes [8] while disassembly of the actin cytoskeleton decreases desmosome resilience [9]. However, the molecular mechanisms by which actomyosin forces alter desmosome structure and function are not understood.

Disruption of the linkage between DP and KIF impairs intercellular adhesion and compromises tissue integrity [10, 11]. Knocking-out keratins leads to elevated phosphorylation of DP, resulting in accelerated endocytosis of desmosomes and rupture of epithelial sheets under rotational stress [12]. Weakening connections between DP and KIF networks dramatically alters the mechanical properties of cells such as cell stiffness and intercellular forces [9]. While these data suggest that

DP is crucial in regulating the response of desmosomes to mechanical stress, the biophysical mechanism by which DP mechanically regulates the desmosome is unknown.

The structure of DP offers hints into its mechanoregulatory function. DP is a large, 2871 amino acid protein which is composed of an N-terminal region, a central rod domain which facilitates DP homodimerization [3], and a C-terminal region which is crucial for aligning and binding KIFs [13]. The N-terminal region of DP is subdivided into a globular head domain and a plakin domain, each playing distinct roles [14]. The globular head domain binds to the C-termini of desmosomal cadherins, and recruits plakophilin and plakoglobin [15]. The plakin domain, characterized by six spectrin repeat (SR) domains interspersed with Src homology (SH) domains, exhibits structural flexibility, as observed in a previous *in vitro*, cell free small angle X-ray scattering study [16]. That investigation revealed that the plakin domain adopts either a folded "U" shape or a fully extended "I" shape, indicating a significant degree of structural adaptability [17]. This suggests that actomyosin forces could induce a conformational change in the N-terminal region of DP, thereby offering a molecular pathway for DP mechanosensitivity. However, force induced conformational changes in DP, particularly within the cell, have never been demonstrated.

Here, we present the first direct evidence for actomyosin force induced conformational changes in the N-terminal region of DP, in human breast cancer MCF7 cells. These cells are enriched with keratin 19 (K19), and we use super-resolution microscopy with wild type (WT), K19-knock out (K19-KO), and K19-GFP rescue (K19-GFP) cells, pharmacological inhibition, co-immunoprecipitation (co-IP), and atomistic Molecular Dynamics (MD) simulations to show that actomyosin forces are directed to DP along K19 filaments. We show that these forces induce a conformational change in the N-terminal plakin domain from a folded ‘closed’ to an extended ‘open’ conformation. Functional adhesion assays show that MCF7 cells with DP in an open conformation are more adhesive than cells with DP in a closed state. Our findings establish, at the molecular level, that DP is a mechanosensor within the desmosome We show that

desmoplakin undergoes a force-induced conformational change which enhances desmosomal mechanical resilience.

Results

K19 remodels desmosome architecture: Desmosomes are characterized by distinct "railroad" track structure, represented by discrete parallel fragments of DP which sandwich the desmosomal cadherins [18]. To validate this signature structure of desmosomes in MCF7 cells, we conducted immunostaining targeting the extracellular region of isoform 2 of desmoglein (Dsg2) and the C-terminal region of DP (DPC) using super-resolution Stimulated Emission Depletion (STED) microscopy. The results, in WT cells, showed well-defined DP "railroad" tracks, as depicted in Fig 1B. To investigate the effect of K19 on desmosome architecture, we used the K19-KO cell line [19]. Successful ablation of K19 in these cells was confirmed using western blots (Fig. S1). Surprisingly, in the K19-KO cells, STED imaging revealed qualitatively more compact desmosomes (Fig. 1C).

Super-resolution microscopy allowed us to visualize the individual DP plaques and quantify the desmosome width by measuring the distance between opposing plaques. To measure distance between opposing plaques, we drew a line scan across the desmosome complex (Fig. 1E) and measured the distance between the two peaks of DPC signal (designated as DPC-DPC distance), as illustrated in the fluorescence intensity plot (Fig. 1F). This quantitative analysis of the desmosome width confirmed our previous observations, with significantly narrower desmosomes formed in the K19-KO cell line (334 ± 61 nm for WT cells and 264 ± 65 nm for K19-KO cells; Fig. 1G).

To corroborate that the observed shift in desmosome width was directly related to the absence of K19, we stably rescued the K19-KO cells with EGFP-tagged K19 (K19-GFP cells). Western blots validated the successful expression of K19-GFP in the rescued cells (Fig. S2). Desmosome width in the K19-GFP cells recovered to a level similar to the WT cell line (322 ± 56; Fig. 1H). Together, these findings show that desmosome architecture in MCF7 cells strongly correlates with the presence/absence of K19. In the presence of K19, the desmosome width is larger, while the desmosome narrows when K19 is knocked out.

Interplay between K19 and the actomyosin networks governs desmosome width: The cytoplasmic KIF network has two distinct components: radial KIFs emanating from the nucleus and anchoring on the desmosomes and the cortical KIFs interconnecting the desmosomes near the plasma membrane [20] (illustrated in Fig. 2A). Interactions between the KIF network and elements of the actomyosin network have been observed at cell-cell junctions and at the cell-substrate interface [8, 21]. To investigate how changes in the KIF network contribute to desmosome remodeling, we first inspected the intracellular localization of K19, DP, and F-actin filaments in K19-GFP cells. K19 was found to form circumferential rims that colocalized with the DP "railroad" tracks along the cell border (Fig. 2B). Additionally, the cortical actin belt was observed to align with the K19 circumferential rim (Fig. 2B). Based on the colocalization of K19 with DP and the coalignment of K19 with F-actin filaments, we hypothesized that K19 interacts with both DP and F-actin filaments.

To validate this hypothesis, we conducted Co-IP experiments using IgG as the control and K19 as the bait protein. The results revealed that K19 interacts with both DP and F-actin, consistent with our previous immunofluorescence microscopy observations (Fig. 2C). In addition,

plakophilin-3, another desmosomal plaque protein, also interacted with K19 (Fig. S3), which further supports the interaction between K19 filaments and the desmosome complex.

It has been demonstrated in Madin-Darby canine kidney (MDCK) cells that knocking down keratin-18 (K18) significantly reduces the formation of force-induced actin stress fibers [22]. Since both K18 and K19 bind to keratin-8 (K8) to form keratin filaments [23], we used confocal fluorescence microscopy to image actin filaments in WT, K19-GFP and K19-KO cells (Fig. S4A). Quantitative analysis of the data showed that compared to WT and K19-GFP cells, actin stress fibers in the K19-KO cells were dramatically decreased (Fig. S4B). This suggests that mechanical tension in the K19-KO cells is lower compared to WT and K19-GFP cells. We therefore hypothesized that actomyosin-generated forces could be transmitted to the desmosome complex through associations with the KIF network.

To test this hypothesis, we used Blebbistatin, a myosin-II-specific ATPase inhibitor, to reduce the actomyosin contractility in the WT cell line and measured the desmosome widths in these Blebbistatin-treated cells (WT+Bleb). A quantitative analysis indicated that Blebbistatin treatment significantly reduced the desmosome width in WT cells to a level that was similar to K19-KO cells (263 ± 62 for WT+Bleb; Fig. 2D). At the same time, the control group treated with Blebbistatin's solvent, dimethyl sulfoxide (DMSO), still retained similar desmosome widths as the WT cells (330 ± 65 for WT+DMSO; Fig. S5). This demonstrates that the K19 dependent change in desmosome architecture are a consequence of a mechanical pathway that is established due to interactions between K19, F-actin, and DP. Consequently, contractile actomyosin forces are transmitted to and reorganize the desmosome, resulting in an increase in desmosome width.

DP elongates in the presence of mechanical force: Since previous studies have reported a structural flexibility in the N-terminal plakin domain of DP [17], we hypothesized that the increase in desmosome width in WT cells was due to a force-induced conformational change in this region of DP (Fig. 3A). To test this, we specifically stained both the DP N-terminal region (DPN) on its globular head domain (which is upstream of the plakin domain) and the extracellular region of Dsg2. We conducted a quantitative comparison of the distances between Dsg2 and DPC, as well as Dsg2 and DPN (as displayed in Fig. 3A), in in both WT and K19-KO cell lines. We selectively measured these distances within the half-unit of the desmosome complex to gain a clearer understanding of the structural changes occurring in a single DP under different conditions. The distances between Dsg2 and DPC were found to be significantly greater in the WT compared to the K19-KO cell line (167 ± 47 for WT cells and 132 ± 50 for K19-KO cells; Fig. 3B). In contrast, no difference was detected in the distances between Dsg2 and DPN in both cell lines (101 ± 48 for WT cells and 99 ± 53 for K19-KO cells; Fig. 3C). As seen in Fig. 3D, the DP length (defined as the distance between DPN and DPC) was 33 nm greater in the WT cells compared to the K19-KO cells, suggesting that DP was elongated by higher mechanical tension in the WT cell lines.

The N-terminal plakin domain transitions from a closed to open conformation when pulled: To resolve the mechanistic basis by which DP transitions between open and closed structures, we proceeded to atomistically simulate the effect of force on the conformation of the highly conserved plakin domain of DP (residues 178-950). We first generated the entire plakin domain structure using Alphfold2 [24]. The predicted structure exhibited a ‘U-shaped’ folded conformation, with spectrin repeat (SR) domains SR3-6 and Src homology (SH) domain SH3 forming a long arm that interacts with a short arm composed of SR7-8 and SR8-CT domains (Fig. 4A). This prediction

agrees well with the crystal structure of the long arm of the plakin domain [25] (RMSD ~1.7Å, Fig. S6).

To identify the interactions crucial for stabilizing the folded conformation, we performed 3 force-independent molecular dynamics (MD) simulations on the predicted structure. The structure stabilized within 20 ns of MD simulation (Fig. S7). During the simulations, 10-15 hydrogen bonds were observed between the long arm and the short arm, and the interactions were mostly observed between SR5-6 and SR7-8 regions (Fig. 4B and Fig. S8). Notably, two consistent salt bridge/hydrogen bond interactions, between four conserved amino acids, were observed across all three simulations: R592-N744 and K444-E858 (Fig. 4A).

To test if the folded plakin domain structure can be unfolded using pulling forces, we performed steered molecular dynamics (SMD) simulations (Video S1). In the SMD simulations, we fixed the position of the N-terminal residues and pulled the C-terminal regions (residues 919-950) using a constant force. Our simulations showed that the plakin domain's long arm and the short arm separated due to the pulling force without secondary structure unfolding (Fig. 4D). Consequently, the plakin domain transitioned from the initial closed (Fig. 4D, left) to the final open (Fig. 4D, right) conformation (Video S1). In the open conformation, the distance between the plakin domain's C-terminus and N-terminus increased by 30~33 nm compared to the closed structure (Fig. 4C), which is consistent with the change in DPC-DPC distance observed in the cell-based experiments (Fig. 3D).

Desmosome adhesion is enhanced when DP is elongated: To examine if elongated DP influences desmosome adhesion, we assessed the intercellular adhesion strength in cell sheets using a dispase assay [26]. In our assay, confluent sheets of cells were detached using dispase

II, a protease that gently cleaves cells from the substrate. Since cell-cell adhesion is mediated via both Ca^{2+}-dependent classical cadherins (like E-cadherin) [27] and desmosomes which adhere in both a Ca^{2+}-independent state and a Ca^{2+} dependent mode [6, 28], we incubated the lifted cell sheets with 4 mM EGTA, a chelating agent for Ca^{2+}, for 1 hour. Consequently, our assay selectively evaluates intercellular adhesion mediated mainly through the Ca^{2+}-independent desmosomes. Following the EGTA treatment, the cell sheets were subjected to mechanical stress, resulting in the fragmentation of the sheets, as shown in Fig. 3E. Our results showed that the K19-KO cell sheets exhibited a significantly greater number of fragments than WT cell sheets. In contrast, K19-GFP cell sheets generated a similar number of fragments compared to WT cell sheets (Fig. 3F). These results indicate that transition of DP from a closed to an open conformation does not compromise intercellular adhesion but instead strengthens adhesion.

Discussion

Our results demonstrate that, in cells, DP senses mechanical forces that are exerted on desmosomes. Using super-resolution microscopy, pharmacological inhibition, and co-IPs, we show that mechanical force generated by the actomyosin cytoskeleton is directed to the desmosome along the KIF network and elongates DP. Atomistic computer simulations show that the elongation of DP is due to a structural transition of the N-terminal plakin domain from a closed to an open conformation. This process is analogous to conformational changes in α-catenin, which associates with classical cadherins in AJs [29-31]. In the case of α-catenin, tension from the actin cytoskeleton induces a conformational change that opens its central M-domain and exposes cryptic binding sites for vinculin and other actin-binding proteins [29-31]. It is likely that force induced opening of DP also exposes cryptic binding sites for junctional proteins that signal and remodel the desmosome and intermediate filaments. The force-induced unfolding of DP could

also serve as a damper of mechanical stress that maintains mechanical homeostasis within tissue.

While desmosomes are known for maintaining the mechanical resilience of tissue, their roles in force transduction are not known. Previous studies in *C. elegans* have demonstrated the importance of VAB-10, a spectraplakin family member, in controlling epidermal morphogenesis [32]. It has been proposed that VAB-10 can change its conformation in response to muscle tension in *C. elegans*, initiating a signaling cascade that leads to the reorganization of intermediate filaments and the maturation of junctions [33]. Since DP is part of the spectraplakin family, it has been proposed that DP may serve a similar role as VAB-10 in mammalian cells [32]. Here, we report of a potential mechanosensitive function of desmosomes in mammalian cells by showing that DP undergoes a conformational change in response to changes in cytoskeletal tension.

Using cells with and without K19 and using inhibitors of myosin-II, we show that actomyosin-generated forces are transmitted to the desmosome via K19 filaments and change desmosome architecture. To confirm that force induced widening of desmosomes did not occur due to differences in desmosomal and cytoskeletal protein expression levels in the different cell lines, we performed a comparative analysis of essential components of the desmosome and cytoskeleton in both WT and K19-KO cells. The results from immunoblotting showed no significant differences in the desmosomal cadherin Dsg2, Dsc1, and Dsc2-3 or plaque proteins plakophilin-1, plakophilin-3, and DP, between the two cell lines (Fig. S1). Likewise, there were no discernable variations observed in cytoskeletal proteins including keratin-8, which is the type II keratin that binds to K19, F-actin, and the myosin heavy chain 10 (Fig. S1). Consequently, these results show that changes in force-induced desmosome organization do not arise from altered protein expression levels, but instead are a consequence of modified mechanical conditions resulting from the cooperative interactions between KIF and the actomyosin network.

Earlier studies using FRET-based tension sensors in resting MDCK cells, revealed a small amount of tension across Dsg2, but not across DP [34, 35]. However, the Dsg2 FRET-based tension sensor showed a higher tension level in the contracting cardiac myocytes, suggesting that junctional tension depends on both cell type and the specific cellular environment [34]. To test the junctional tension in MDCK cells and validate our analysis, we measured DPC-DPC distances in resting MDCK cells. Our quantitative analysis reveals that the desmosome width in MDCK cells is comparable to that observed in K19-KO cells implying that DP in MDCK cells indeed does not undergo conformational changes under low forces (Fig. S9).

Keratin deficiency is known to significantly affect cellular function, leading to impaired intercellular adhesion and increased invasiveness [6, 36, 37]. In agreement, results of our dispase assay show that intercellular adhesion strength is considerably reduced in K19-KO cells. It is important to highlight that our data eliminates the adhesive contribution of Ca^{2+} dependent AJs, since we chelate out the free Ca^{2+} using EGTA prior to shearing the cell sheets. A previous study which measured total E-cadherin levels in K19-KO MCF7 cells, reported that E-cadherins are internalized in these cells, which results in reduced cell-cell adhesion [19]. However, when we quantitatively compared the E-cadherins expressed on the surface of WT and K19-KO cells using immunofluorescence, we only found a slight decrease in E-cadherin expression levels (Fig. S10A). Furthermore, we tested if the 'amount' of desmosomes in the WT and K19-KO cells were similar. To accomplish this, we measured the desmosome line density (*i.e.* $\frac{desmosome\ length}{cell}$). Line density is a better metric for quantifying desmosome 'amounts' rather than $\frac{\#\ of\ desmosomes}{cell}$, since different desmosomes have different lengths. We measured the desmosome line density in WT and K19-KO cells by measuring the DP length along the cell borders in the respective cell lines. The results showed a slight decrease in desmosome line density in the K19-KO cells compared to the WT cells (Fig. S10B). While the desmosome line density in these cell lines were only marginally different, it is important to recognize that they could also contribute to the impaired

adhesion exhibited by the K19-KO cells. One possible reason for the reduction in desmosome line density in K19-KO cells is that keratin deficiency has been reported to cause faster endocytosis of desmosomes through elevated DP phosphorylation [12].

Previous SMD simulations carried out on the long arm of the plakin domain (i.e. the crystal structure with PDB code 3R6N [25]), show that the SRs individually unfold when subjected to pulling force, which exposes the SH3 domain [38, 39]. Since our simulations are carried out on the entire plakin domain, which includes the flexible hinge between the long and short arms, we capture the transition of the plakin domain from a closed to an open conformation. The conformational change that we measure is supported by previous SAXS measurements [17]. However the transition of the plakin domain from a closed to an open structure also partially exposes the cryptic SH3 domain which is known to act as a signal transduction adapter crucial in cell invasiveness, migration, and actin reorganization [40].

Many disease-causing mutations in DP are found within the plakin domain of the N-terminal region, affecting residues both hidden within the protein and exposed to the surrounding environment [41]. Specifically, mutations within the SR7-8 region of the plakin domain have been linked to arrhythmogenic ventricular cardiomyopathy (AVC) [16, 41]. Importantly, our simulations predict that the SR7-8 region participates in several key hydrogen bonds with SR5-6, which in turn stabilizes DP in its closed conformation. This raises the possibility that AVC mutations may interfere with the force induced structural transition of DP from the closed to the open conformation.

Materials and Methods

Cell culture and stabilization: MCF7 WT cells (ATCC), MCF7 K19-KO cells, and MCF7 K19-GFP rescued cells were maintained in low-glucose Dulbecco's Modified Eagle's Medium (DMEM) (Gibco) supplemented with 10% Fetal Bovine Serum (FBS) (Life Technologies) and 1% penicillin–streptomycin (Sigma-Aldrich) in 5% CO2 at 37°C. The rescued cells were additionally treated with 100 ug/ml hygromycin for selection of K19-GFP. MDCK cells (ATCC) were cultured in low glucose DMEM (Gibco) cell culture media with 10% FBS and 1% PSK.

The K19-KO cells were generated using the CRISPR/Cas9 technology as previously described [42].We developed the K19-GFP rescue cell line following protocols described previously [43]. Briefly, K19-GFP was cloned into *K*19-KO cells from pEGFP-K19 plasmid into pLenti CMV Hygro (plasmid #17484. Addgene) using the following primers: forward 5'TCAGTCGACTGGATCCATGGTGAGCAAGGGCGAGG3' and reverse 5'GAAAGCTGGGTCTAGTCAGAGGACCTTGGAGGC3'. Lentiviral supernatants were generated using pLenti-K19-GFP plasmid. Lentiviral supernatants collected 24h post-transfection was used to infect subconfluent K19-KO cells in three sequential 4 h incubations in the presence of 4 ug/ml polybrene (Sigma-Aldrich). Transductants were selected using a culture medium containing 100 ug/ml hygromycin beginning 48h after infection. The K19-GFP rescue cells were further stabilized using fluorescence-activated cell sorting.

Preparation of imaging samples: Approximately 500,000 cells were seeded for all the MCF7 cell lines and approximately 250,000 cells were seeded for MDCK cells on the collagen-coated coverslips (22 mm, No.1.5) in a single well of a six-well plate and were kept in 5% CO2 at 37°C for 24 h. A ‘calcium switch’ was then performed using the protocol described below to eliminate cell clusters and maintain a similar level of desmosome maturation across all samples. To perform a calcium switch, the cells were first rinsed with phosphate-buffered saline (PBS) (Gibco) solution

at room temperature, followed by incubation in 4 mM EGTA (Millipore Sigma) and 10% low Ca^{2+} Fetal Bovine Serum (FBS) in Ca^{2+}-free DMEM for 30 min. Following EGTA treatment, the cells were switched to a DMEM medium with 2 mM $CaCl_2$ for 24 h to trigger formation of mature desmosomes.

WT+Bleb cells were treated with 50 μM (±) blebbistatin (Millipore Sigma) for 24 h. The blebbistatin was dissolved in DMSO and diluted in a complete medium. The control group was prepared with the same protocol but treated with 0.1% DMSO instead. Next, cells were fixed either with ice-cold 1:1 methanol and acetone for 10 min (for keratin and DP staining) or with 3% PFA and 0.3% Triton X-100 for 10 min at room temperature (RT) (for F-actin staining). Samples were rinsed with PBS three times and blocked in 1% Bovine Serum Albumin (BSA) overnight at 4°C. Samples were then incubated with primary antibody (1:200) for 1 h at RT, followed by incubation with secondary antibody (1:600) for 30 min at RT. The samples stained with fluorescently labeled phalloidin (1:400) were incubated with phalloidin for 30 min at RT in the dark. Samples were washed three times with PBS after each antibody incubation. Lastly, samples were mounted to the glass slides using the ProLong Diamond Antifade Mountant (Life Technologies) and stored at 4°C in the dark.

Antibodies: The following primary antibodies were used: human anti-DSG2 (MAB947, R&D systems), rabbit anti-DPC antibody (A303-356A, Bethyl Lab), rabbit anti-DPN antibody (25318-1-AP, Proteintech), chicken anti-GFP (600-901-215, Rockland), mouse anti-K19 antibody (A53-B/A2) (Santa Cruz Biotechnology), control mouse IgG (sc-2025) (Santa Cruz Biotechnology), and mouse anti-actin antibody (66009-1-Ig, Proteintech). The following secondary antibodies are used: anti-chicken AF-488 (Invitrogen), anti-mouse AF-594 (Invitrogen), and anti-rabbit AF-647 (Invitrogen). Phalloidin AF-568 (Invitrogen) was used for F-actin staining.

STED imaging acquisition and processing: Immunofluorescence images were acquired at RT using a Leica TCS SP8 STED 3X confocal microscope (Leica Microsystems) equipped with a 100-x oil immersion objective (HC PL APO CS2), white light laser for excitation lines between 470-670 nm, and depletion laser lines at 592, 660, and 775 nm. The acquisition was performed using LasX software, followed by deconvolution in Huygens Pro software (Scientific Volume Imaging). Post-acquisition processing, including cropping and resizing, color change in the lookup table, adjustment of brightness and contrast, and inversion of grayscale images, was performed using the ImageJ software.

Confocal image acquisition and processing: Immunofluorescence images were acquired using a Leica Stellaris 5 confocal microscope (Leica Microsystems) equipped with 63x oil immersion objective (HC PL APO CS2). Image acquisition was performed using LasX software, followed by post-processing using ImageJ. During post-processing, images were adjusted with inversion of grayscale, enhanced contrast with 0.3% saturated pixels, and reduced background noise using the despeckle functionality. All images were acquired using the same procedure.

Image analysis: We used custom-made ImageJ macros and Python scripts to quantify the desmosome width along the entire cell-cell border. Since Dsg2 signals colocalize between DP "railroad" tracks, they were used as the reference to indicate desmosome location along the membrane. Briefly, Dsg2 signals were selected as regions of interest (ROIs), and an algorithm was used to determine the midline of the ROIs along the membrane axis and draw a segment along the midline, every 200 nm, to obtain the intensity profile of both Dsg2 and DPC or Dsg2 and

DPN. Then, Bar, an ImageJ Plugin, was used to determine the location of peaks of different signals in their respective channels along the drawn segment. After obtaining the raw data, we used custom-made MATLAB code to calculate distances for full desmosome width represented by DPC-DPC or half desmosome width represented by Dsg2-DPC or Dsg2-DPN. To avoid false signals resulting from background noise or lines not fully drawn over the DP "railroad" track, we filtered out the data that showed less or more than two peaks in the DPC signals along the drawn segment or did not have the Dsg2 signal between the two DPC peaks. Furthermore, in certain desmosomes, the Dsg2 signals were observed as two peaks, as shown in Fig. S11A-B, implying that the desmosome had ruptured at the Dsg2 extracellular region. We eliminated these desmosomes from further analysis and only focused on intact desmosomes with unresolvable Dsg2 signals, as depicted in Fig. 1F. For the DP line density measurement, we also used a custom-made ImageJ macro script for the quantitative analysis. Briefly, we first subtracted the background noise while retaining the DP signals along the cell borders. Then, we skeletonized these signals into segments to obtain the total amount of DP length along cell borders. Lastly, we obtained the DP line density by normalizing the total DP length using the number of cells in the image (*i.e.* $\frac{desmosome\ length}{cell}$).

Co-immunoprecipitation: Co-immunoprecipitation was performed as described previously [44]. Cells grown on tissue culture plates were washed three times with 1X cold PBS. Cells were lysed at 4°C using ice-cold 1% triton lysis buffer (1% Triton X-100, 40mM HEPES (pH 7.5), 120mM NaCl, 1mM EDTA, 1mM phenylmethylsulfonyl fluoride, 10mM sodium pyrophosphate, 1 µg/ml each of chymostatin, leupeptin and pepstatin, 10 µg/ml each of aprotinin and benzamidine, 2 µg/ml antipain, 1mM sodium orthovanadate, 50mM NaF). Cell lysates were centrifuged to remove cellular debris, and protein concentration was determined using Pierce BCA Protein Assay Kit

and BSA as standards. Cell lysates were pre-cleared using Protein G Plus-Agarose beads (Santa Cruz Biotechnology) for 40 minutes at 4°C while rotating. While rotating, supernatants were incubated with the indicated antibody or IgG control for two hours at 4°C. Immuno-complexes were captured using Protein G Plus-Agarose beads and washed 4X using 1% triton lysis buffer supplemented with 300 mM NaCl.

Gel electrophoresis and immunoblotting: Cells grown on tissue culture plates were washed three times with 1X cold PBS. Cells were lysed at 4°C using ice-cold 1% triton lysis buffer (1% Triton X-100, 40mM HEPES (pH 7.5), 120mM NaCl, 1mM EDTA, 1mM phenylmethylsulfonyl fluoride, 10mM sodium pyrophosphate, 1 µg/ml each of chymostatin, leupeptin and pepstatin, 10 µg/ml each of aprotinin and benzamidine, 2 µg/ml antipain, 1mM sodium orthovanadate, 50mM NaF). For immunoblotting, cell lysates were centrifuged at 14,000rpm for 5 minutes at 4°C to remove cellular debris. Protein concentration was determined using the Pierce BCA Protein Assay Kit following manufacturer's instructions (WG327385. Thermo Scientific). BSA (Equitech-Bio) prepared in 1% lysis buffer was used as the standard. Aliquots of protein lysates were resolved using SDS-PAGE and then transferred to nitrocellulose membranes (0.45um) (Amersham Protran; Cytiva) and immunoblotted using the indicated antibodies, followed by horseradish peroxidase-conjugated goat anti-mouse or goat anti-rabbit IgG (Sigma-Aldrich). Western Lightning Plus-ECL (Waltham, MA) or Amersham ECL Select Western was used as blotting detection reagent. Signals were detected using iBright™ CL1500 Imaging System, Invitrogen (Thermo Fisher Scientific). The immunoblot result for comparing K19 levels among the three cell lines was conducted with a different method, as described previously [45].

Dispase assay: Cells were seeded in the tissue-treated well of a 12-well plate (1000,000 cells/well) and grown for 24 h to form a confluent cell sheet. Then, the cell sheets were detached using 2.4 U/ml dispase II (Millipore Sigma) buffer for 30 min at 37°C. Detached cell sheets were treated with 4 mM EGTA for 1h at RT. During the incubation, images of the cell sheet in each well were obtained using a Leica TCS SP8 confocal microscope with a 10x 0.4 dry objective (HC PL APO CS2). Since the field of view for each image is small, each well was selected as an ROI. In the navigation mode, tiles of images were taken individually and stitched together during acquisition to eventually cover the entire ROI and generate the image of cell sheets in the wells. After the EGTA incubation, cell sheets were subjected to mechanical stress using an orbital shaker at 200 rpm for 1 min. Cell fragments in each well were imaged as previously described, and the images were later used to count the number of fragments.

Statistical analysis: All statistical tests were performed using GraphPad Prism (GraphPad Software), and all graphs were plotted using custom-made Python code. In the boxplots, the box represents the 25th and 75th percentiles with the median indicated, and whiskers reach the 1.5 times the interquartile range (IQR), defined as the difference between the 25th and 75th percentiles. Data points outside the whiskers are shown as outliers. The number of independent experiments (N) and data points (n) is indicated in each figure legend. Data distribution was first tested based on Shapiro-Wilk's test. Since most data was not normally distributed, non-parametric statistic tests were used for the analysis. Data were analyzed using Mann-Whitney's U test. A multiple-group comparison was performed using the Kruskal-Wallis Test, followed by Dunn's multiple comparison Test. Statistical tests used are specified in the figure legends. Statistical significance was represented at the level of *, $P < 0.05$; **, $P < 0.01$; ***, $P<0.001$; ns, $P>0.05$.

454 **Structure preparation and MD simulation:** Plakin domain structure (residues 178-950) was
455 predicted using Alphafold2 [24]. Subsequently, the structure was prepared using PDBFixer [46]
456 and missing hydrogens were added under pH 7.0 conditions. The protein N-terminus was
457 designated with "NH3+" while "COO-" was assigned to the C-terminus. MD simulations were
458 conducted on the FARM high-performance computing cluster at University of California, Davis
459 with GROMACS 2022.3 as previously described [47]. The simulations were performed in OPLS-
460 AA/L force field [48] and TIP4P water model with 10 Å radius cut-off for Van der Waals and
461 electrostatic interactions. Electrostatic energy calculations employed the particle mesh Ewald
462 method with a 0.16-grid spacing. At the beginning of the simulation, the plakin domain structure
463 was positioned at the center of a dodecahedral box, ensuring a minimum distance of 1 nm from
464 the boundary for every atom. The box was filled with water molecules and neutralized with
465 charged ions (150 mM NaCl, 4 mM KCl, and 2 mM $CaCl_2$). The system was relaxed with energy
466 minimization and stabilized with equilibration under isothermal-isochoric and isothermal isobaric
467 conditions using a modified Berendsen thermostat and Berendsen barostat. Post-stabilization, a
468 50 ns MD simulation was performed with 2-fs integration steps maintaining a temperature of 300K
469 using a v-rescale thermostat. Equilibration of the protein structure occurred within 20 ns. The
470 number of hydrogen bonds observed between the long arm and the short arm was calculated
471 using *gmx hbond*.

472

473 **Constant-force SMD simulations and analysis:** The constant force SMD simulations were
474 performed as described previously [47]. The starting structures for the SMD simulations were the
475 last frame of the corresponding MD simulations. The structures were placed at the side of a
476 rectangular box (23 × 70 × 8 nm box, center at [11.5nm, 65nm, 4nm]). The system, containing
477 ~1,600,000 atoms was relaxed and equilibrated under isothermal-isobaric conditions using the
478 same protocol as in the MD simulation. The SMD simulations were performed at 310K

479 temperature using a Nose-Hoover thermostat [49]. During each SMD simulation, we fixed the C-
480 terminus of the plakin domain and pulled the N-terminal region (residues 919-950) along the
481 longest axis of the box with a constant force ~830 pN (500 kJ·mol−1·nm−1). The distances
482 between protein N-terminal and C-terminal were calculated using *gmx pairdist*.

483

484 **Acknowledgments:** Research in the SS lab was supported by the National Institute of General
485 Medical Sciences of the National Institutes of Health (R01GM121885). Research in the JSC lab
486 was supported by the National Institute of General Medical Sciences of the National Institutes of
487 Health (R15CA267890-01). STED imaging was performed at the UC Davis Advanced Imaging
488 Facility. FACS was performed at the Flow Cytometry Shared Resource funded by the UC Davis
489 Comprehensive Cancer Center Support Grant (CCSG) awarded by the National Cancer Institute
490 (NCI P30CA093373).

491

492 **Data availability:** STED, Co-IP, and MD simulation data are made available in the manuscript
493 and supporting information.

494

495 **Conflict of Interest Statement:** The authors do not declare any competing interests.

496

497 **References**

498 1. Green, K.J. and C.L. Simpson, *Desmosomes: New Perspectives on a Classic.* Journal of
499 Investigative Dermatology, 2007. **127**(11): p. 2499-2515.

500 2. Broussard, J.A., S. Getsios, and K.J. Green, *Desmosome regulation and signaling in*
501 *disease.* Cell and Tissue Research, 2015. **360**(3): p. 501-512.

502 3. Garrod, D. and M. Chidgey, *Desmosome structure, composition and function.* Biochim
503 Biophys Acta, 2008. **1778**(3): p. 572-87.

504 4. Stahley, S.N. and A.P. Kowalczyk, *Desmosomes in acquired disease.* Cell and Tissue
505 Research, 2015. **360**(3): p. 439-456.

506 5. Holthofer, B., et al., *Structure and function of desmosomes.* Int Rev Cytol, 2007. **264**: p.
507 65-163.

508 6. Hatzfeld, M., R. Keil, and T.M. Magin, *Desmosomes and Intermediate Filaments: Their*
509 *Consequences for Tissue Mechanics.* Cold Spring Harbor Perspectives in Biology, 2017.
510 **9**(6): p. a029157.

511 7. Broussard, J.A., et al., *Scaling up single-cell mechanics to multicellular tissues – the role*
512 *of the intermediate filament–desmosome network.* Journal of Cell Science, 2020. **133**(6):
513 p. jcs228031.

514 8. Prechova, M., et al., *Plectin-mediated cytoskeletal crosstalk controls cell tension and*
515 *cohesion in epithelial sheets.* Journal of Cell Biology, 2022. **221**(3).

516 9. Broussard, J.A., et al., *The desmoplakin-intermediate filament linkage regulates cell*
517 *mechanics.* Mol Biol Cell, 2017. **28**(23): p. 3156-3164.

518 10. Huen, A.C., et al., *Intermediate filament–membrane attachments function synergistically*
519 *with actin-dependent contacts to regulate intercellular adhesive strength.* The Journal of
520 Cell Biology, 2002. **159**(6): p. 1005-1017.

521 11. Bornslaeger, E.A., et al., *Breaking the connection: displacement of the desmosomal*
522 *plaque protein desmoplakin from cell-cell interfaces disrupts anchorage of intermediate*
523 *filament bundles and alters intercellular junction assembly.* The Journal of cell biology,
524 1996. **134**(4): p. 985-1001.

525 12. Kröger, C., et al., *Keratins control intercellular adhesion involving PKC-α–mediated*
526 *desmoplakin phosphorylation.* Journal of Cell Biology, 2013. **201**(5): p. 681-692.

527 13. Stappenbeck, T.S., et al., *Phosphorylation of the desmoplakin COOH terminus*
528 *negatively regulates its interaction with keratin intermediate filament networks.* J Biol
529 Chem, 1994. **269**(47): p. 29351-4.

530 14. Jefferson, J.J., et al., *Structural analysis of the plakin domain of bullous pemphigoid*
531 *antigen1 (BPAG1) suggests that plakins are members of the spectrin superfamily.*
532 Journal of Molecular Biology, 2007. **366**(1): p. 244-257.

533 15. Smith, E.A. and E. Fuchs, *Defining the interactions between intermediate filaments and*
534 *desmosomes.* Journal of Cell Biology, 1998. **141**(5): p. 1229-1241.

535 16. Al-Jassar, C., et al., *The nonlinear structure of the desmoplakin plakin domain and the*
536 *effects of cardiomyopathy-linked mutations.* J Mol Biol, 2011. **411**(5): p. 1049-61.

537 17. Al-Jassar, C., et al., *Hinged Plakin Domains Provide Specialized Degrees of Articulation*
538 *in Envoplakin, Periplakin and Desmoplakin.* PLoS ONE, 2013. **8**(7): p. e69767.

539 18. Stahley, S.N., et al., *Molecular organization of the desmosome as revealed by direct*
540 *stochastic optical reconstruction microscopy.* Journal of Cell Science, 2016. **129**(15): p.
541 2897-2904.

542 19. Alsharif, S., et al., *Keratin 19 maintains E-cadherin localization at the cell surface and*
543 *stabilizes cell-cell adhesion of MCF7 cells.* Cell Adhesion & Migration, 2021. **15**(1): p. 1-
544 17.

545 20. Quinlan, R.A., et al., *A rim-and-spoke hypothesis to explain the biomechanical roles for*
546 *cytoplasmic intermediate filament networks.* Journal of Cell Science, 2017. **130**(20): p.
547 3437-3445.

548 21. Leube, R.E., M. Moch, and R. Windoffer, *Intermediate filaments and the regulation of*
549 *focal adhesion.* Curr Opin Cell Biol, 2015. **32**: p. 13-20.

550 22. Fujiwara, S., et al., *Interplay between Solo and keratin filaments is crucial for mechanical*
551 *force-induced stress fiber reinforcement.* Mol Biol Cell, 2016. **27**(6): p. 954-66.

552 23. Snider, N.T., et al., *Keratin hypersumoylation alters filament dynamics and is a marker*
553 *for human liver disease and keratin mutation.* J Biol Chem, 2011. **286**(3): p. 2273-84.

554 24. Jumper, J., et al., *Highly accurate protein structure prediction with AlphaFold.* Nature,
555 2021. **596**(7873): p. 583-589.

556 25. Choi, H.-J. and W.I. Weis, *Crystal Structure of a Rigid Four-Spectrin-Repeat Fragment of*
557 *the Human Desmoplakin Plakin Domain.* Journal of Molecular Biology, 2011. **409**(5): p.
558 800-812.

559 26. Hobbs, R.P., et al., *The calcium ATPase SERCA2 regulates desmoplakin dynamics and*
560 *intercellular adhesive strength through modulation of PKCα signaling.* The FASEB
561 Journal, 2011. **25**(3): p. 990-1001.

562 27. Mendonsa, A.M., T.-Y. Na, and B.M. Gumbiner, *E-cadherin in contact inhibition and*
563 *cancer.* Oncogene, 2018. **37**(35): p. 4769-4780.

564 28. Thomason, A., Helen, et al., *Desmosomes: adhesive strength and signalling in health*
565 *and disease.* Biochemical Journal, 2010. **429**(3): p. 419-433.

566 29. Yao, M., et al., *Force-dependent conformational switch of α-catenin controls vinculin*
567 *binding.* Nature Communications, 2014. **5**(1).

568 30. Kim, T.-J., et al., *Dynamic Visualization of α-Catenin Reveals Rapid, Reversible*
569 *Conformation Switching between Tension States.* Current Biology, 2015. **25**(2): p. 218-
570 224.

571 31. Yonemura, S., et al., *α-Catenin as a tension transducer that induces adherens junction*
572 *development.* Nature Cell Biology, 2010. **12**(6): p. 533-542.

573 32. Gillard, G., et al., *Force Transmission between Three Tissues Controls Bipolar Planar*
574 *Polarity Establishment and Morphogenesis.* Curr Biol, 2019. **29**(8): p. 1360-1368 e4.

575 33. Zhang, H., et al., *A tension-induced mechanotransduction pathway promotes epithelial*
576 *morphogenesis.* Nature, 2011. **471**(7336): p. 99-103.

577 34. Baddam, S., et al., *The desmosomal cadherin desmoglein-2 experiences mechanical*
578 *tension as demonstrated by a FRET-based tension biosensor expressed in living cells.*
579 Cells, 2018. **7**(7): p. 66.

580 35. Price, A.J., et al., *Mechanical loading of desmosomes depends on the magnitude and*
581 *orientation of external stress.* Nature Communications, 2018. **9**(1).

582 36. Seltmann, K., et al., *Keratins significantly contribute to cell stiffness and impact invasive*
583 *behavior.* Proceedings of the National Academy of Sciences, 2013. **110**(46): p. 18507-
584 18512.

585 37. Cheung, J., Kevin, et al., *Collective Invasion in Breast Cancer Requires a Conserved*
586 *Basal Epithelial Program.* Cell, 2013. **155**(7): p. 1639-1651.

587 38. Daday, C., K. Kolšek, and F. Gräter, *The mechano-sensing role of the unique SH3*
588 *insertion in plakin domains revealed by Molecular Dynamics simulations.* Scientific
589 Reports, 2017. **7**(1).

590 39. Rief, M., et al., *Single molecule force spectroscopy of spectrin repeats: low unfolding*
591 *forces in helix bundles.* Journal of molecular biology, 1999. **286**(2): p. 553-561.

592 40. Kurochkina, N. and U. Guha, *SH3 domains: modules of protein–protein interactions.*
593 Biophysical Reviews, 2013. **5**(1): p. 29-39.

594 41. Ortega, E., et al., *The Structure of the Plakin Domain of Plectin Reveals an Extended*
595 *Rod-like Shape.* Journal of Biological Chemistry, 2016. **291**(36): p. 18643-18662.

596 42. Sharma, P., et al., *Keratin 19 regulates cell cycle pathway and sensitivity of breast*
597 *cancer cells to CDK inhibitors.* Scientific Reports, 2019. **9**(1).

598 43. Sharma, P., et al., *Keratin 19 interacts with GSK3beta to regulate its nuclear*
599 *accumulation and degradation of cyclin D3.* Mol Biol Cell, 2021. **32**(21): p. ar21.

600 44. Fallatah, A., et al., *Keratin 19 binds and regulates cytoplasmic HNRNPK mRNA targets*
601 *in triple-negative breast cancer.* BMC Molecular and Cell Biology, 2023. **24**(1).

45. Shafraz, O., C.M.O. Davis, and S. Sivasankar, *Light-activated BioID – an optically activated proximity labeling system to study protein–protein interactions.* Journal of Cell Science, 2023. **136**(19).

46. Eastman, P., et al., *OpenMM 7: Rapid development of high performance algorithms for molecular dynamics.* PLoS Comput Biol, 2017. **13**(7): p. e1005659.

47. Xie, B., et al., *Strengthening E-cadherin adhesion via antibody-mediated binding stabilization.* Structure, 2024. **32**(2): p. 217-227 e3.

48. Kaminski, G.A., et al., *Evaluation and reparametrization of the OPLS-AA force field for proteins via comparison with accurate quantum chemical calculations on peptides.* Journal of Physical Chemistry B, 2001. **105**(28): p. 6474-6487.

49. Lemkul, J.A. and D.R. Bevan, *Assessing the stability of Alzheimer's amyloid protofibrils using molecular dynamics.* J Phys Chem B, 2010. **114**(4): p. 1652-60.

Figure Legends

Fig. 1: Keratin-19 influences desmosome architecture. (A) Schematic of desmosome structure. **(B-D)** Representative STED images of desmosomes showing a characteristic 'railroad track' pattern in **(B)** MCF7 WT cells, **(C)** MCF7 K19-KO cells, and **(D)** MCF7 K19-GfP cells. The desmosomes were immunolabeled for DPC (green) and Dsg2 (red). Scale bar: 500 nm. **(E)** The boxed area from the representative STED images of MCF7 WT cells shows a closer look at an individual DP railroad track with Dsg2 between the two parallel DP plaques. Scale bar: 200 nm. **(F)** Line-scan analysis of DPC and Dsg2 fluorescence intensity (indicated by the dashed line in E). **(G)** Quantification of DPC-DPC distance from WT and K19-KO cells showing that

desmosomes in WT cells are wider than K19-KO cells. In all boxplots, the box represents the 25th and 75th percentiles with the median indicated and whiskers reach 1.5 times the interquartile range (IQR), defined as the difference between the 25th and 75th percentiles. Data points outside the whiskers are shown as outliers. Number of datapoints (n) = 630 (WT), 505 (K19-KO); Number of replicates (N) = 3. Mann-Whitney's U test; ***, P<0.001. **(H)** Quantification of DPC-DPC distance in K19-KO, WT, and K19-GFP cells. Desmosomes in WT and K19-GFP cells are wider than K19-KO cells. n = 505 (K19-KO), 630 (WT), 716 (K19-GFP); N = 3. Kruskal-Wallis Test, followed by Dunn's multiple comparison Test; ***, P<0.001.

Fig. 2: Interplay between keratin-19 and actomyosin network determine desmosome width. **(A)** Schematic of the interactions between the desmosome, K19 filaments, and actin filaments. Cortical filaments represent keratin rims and actin belts below the plasma membrane. Radial filaments represent the keratin filaments that anchor at the desmosome and extend into the cell. The radial filaments interact with cortical filaments. **(B)** Representative STED images of K19-GFP rescue cells immunolabeled for K19 (magenta), DP (green), and actin (cyan). The individual component is shown in grayscale to highlight the structural features. The merged images between K19 and DP or actin are shown at the right. Scale bar: 500 nm. The images show that K19 circumferential rims colocalize with the DP "railroad" tracks and with cortical actin belts. **(C)** Co-IP of K19 in WT cells. IP was performed with anti-K19 antibody or IgG control. The Co-Ips show that K19 interacts with both DP and F-actin. **(D)** Quantification of desmosome widths from WT, K19-KO, and Blebbistatin-treated WT (WT+Blebb) cells showing that Blebbistatin treatment reduces the desmosome width to a similar level as in the K19-KO cell line. n = 630 (WT), 505 (K19-KO), 650 (WT+Blebb); N = 3. Kruskal-Wallis Test, followed by Dunn's multiple comparison Test; ***, P<0.001.

Fig. 3: Desmoplakin undergoes force induced conformational change. (A) Schematic of the desmosome under tension. The N-terminal of DP transitions from a closed conformation to an open conformation. **(B)** Quantification of desmosome half-unit widths (Dsg2-DPC distance) from WT and K19-KO cells. n = 1260 (WT), 1010 (K19-KO); N = 3. Mann-Whitney's U test; ***, P<0.001. The distances between Dsg2 and DPC is significantly greater in the WT compared to the K19-KO cells. **(C)** Quantification of desmosome half-unit widths (Dsg2-DPN distance) from WT and K19-KO cells. n = 692 (WT), 826 (K19-KO); N = 3. Mann-Whitney's U test; ns, P>0.05. The Dsg2-DPN distance in both cell lines are similar. **(D)** The mean values from the results in B and C are summarized in the bar chart to compare the DP length (DPN-DPC distance) between the WT and K19-KO cells. The DP length is 66 nm for the WT and 33 nm for the K19-KO, indicating that DP extends 33 nm in the WT cells. **(E)** Dispase assay after 24 h plating. The confluent cell sheets are treated with 4 mM EGTA for 1 h. The images show the intact cell sheets for WT, K19-KO, and K19-GFP rescued cells before stress and fragmented cell sheets after applying mechanical stress. **(F)** Quantification of the dispase assay from K19-KO, WT, and K19-GFP cells. n = 12 (KO), 12 (WT), 9 (K19-GFP); N = 3. Kruskal-Wallis Test, followed by Dunn's multiple comparison Test; ***, P<0.001. The K19-KO cell sheets show a greater number of fragments compared to WT cell sheets, while K19-GFP cell sheets generate a similar number of fragments as WT. This indicates that elongation of DP strengthens intercellular adhesion in WT and K19-GFP cells.

Fig. 4: Molecular Dynamics simulations reveal force-induced changes in plakin domain conformation. (A) The entire plakin domain structure predicted by Alphafold2, suggesting a U-shape conformation in the absence of force. Two common electrostatic interactions (R592-N744,

672 and K444-E858) observed in all 3 MD simulations (below) are shown. **(B)** During the MD
673 simulations, 10 to 15 hydrogen bonds were formed between plakin domain's long arm (SR3-4
674 and SR5-6) and short arm (SR7-8 and SR8-CT). **(C)** During the SMD simulations, distance
675 between plakin domain's C-terminus and N-terminus was measured, suggesting the structure has
676 been elongated by 30~33 nm. This elongation correlates with the distance change experimentally
677 measured in Fig 3. **(D)** Comparison of the plakin domain structure at the start (left) and at the end
678 (right) of the SMD simulation. The structures show that the overall plakin domain has been
679 elongated by the pulling force without significant secondary structure unfolding.

Figure 1

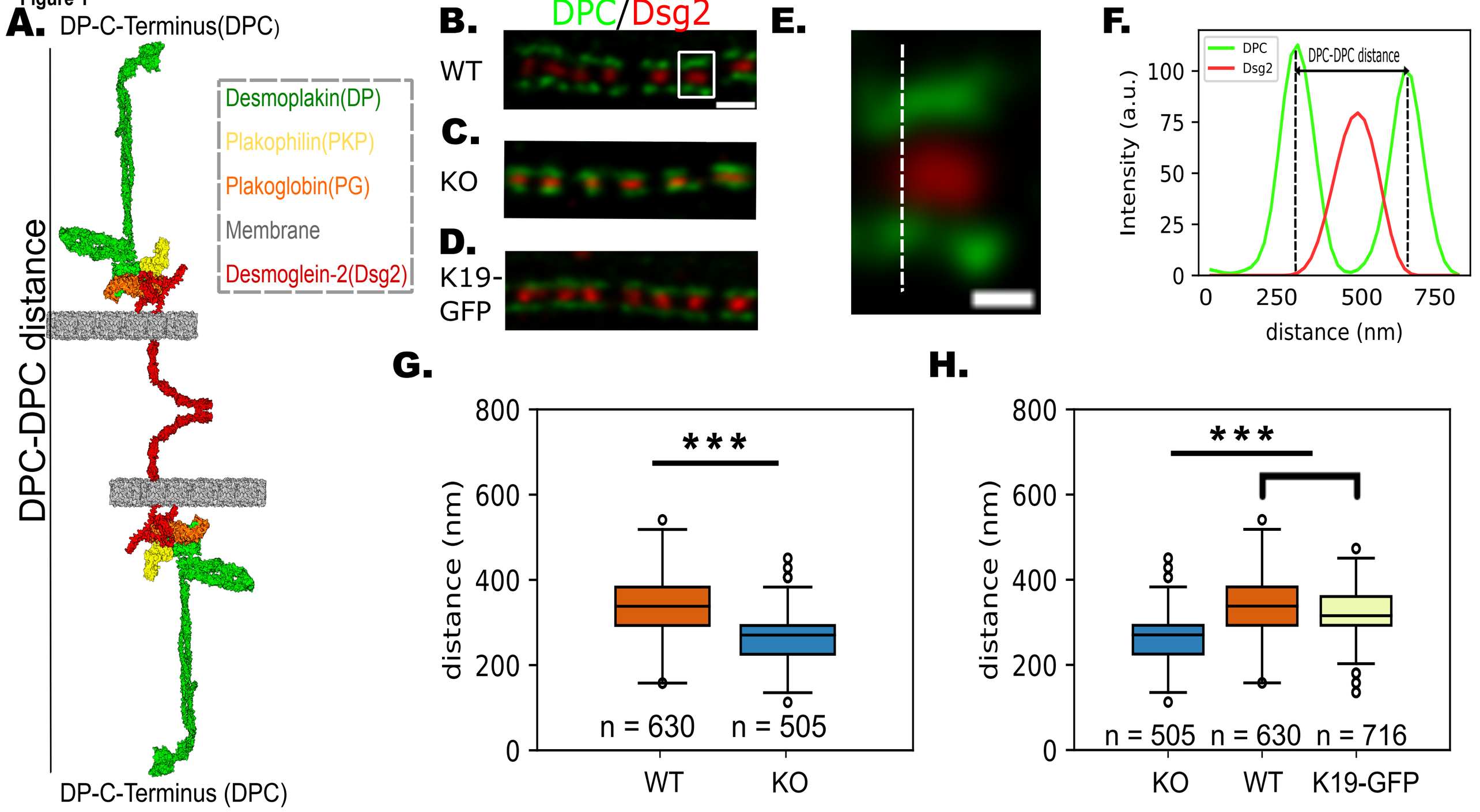
A.
DP-C-Terminus(DPC)
Desmoplakin(DP)
Plakophilin(PKP)
Plakoglobin(PG)
Membrane
Desmoglein-2(Dsg2)
DPC-DPC distance
DP-C-Terminus (DPC)
B.
DPC/Dsg2
WT
C.
KO
D.
K19-GFP
E.
F.
DPC
Dsg2
DPC-DPC distance
Intensity (a.u.)
distance (nm)
G.
***
distance (nm)
n = 630
n = 505
WT
KO
H.
***
distance (nm)
n = 505
n = 630
n = 716
KO
WT
K19-GFP

Figure 2

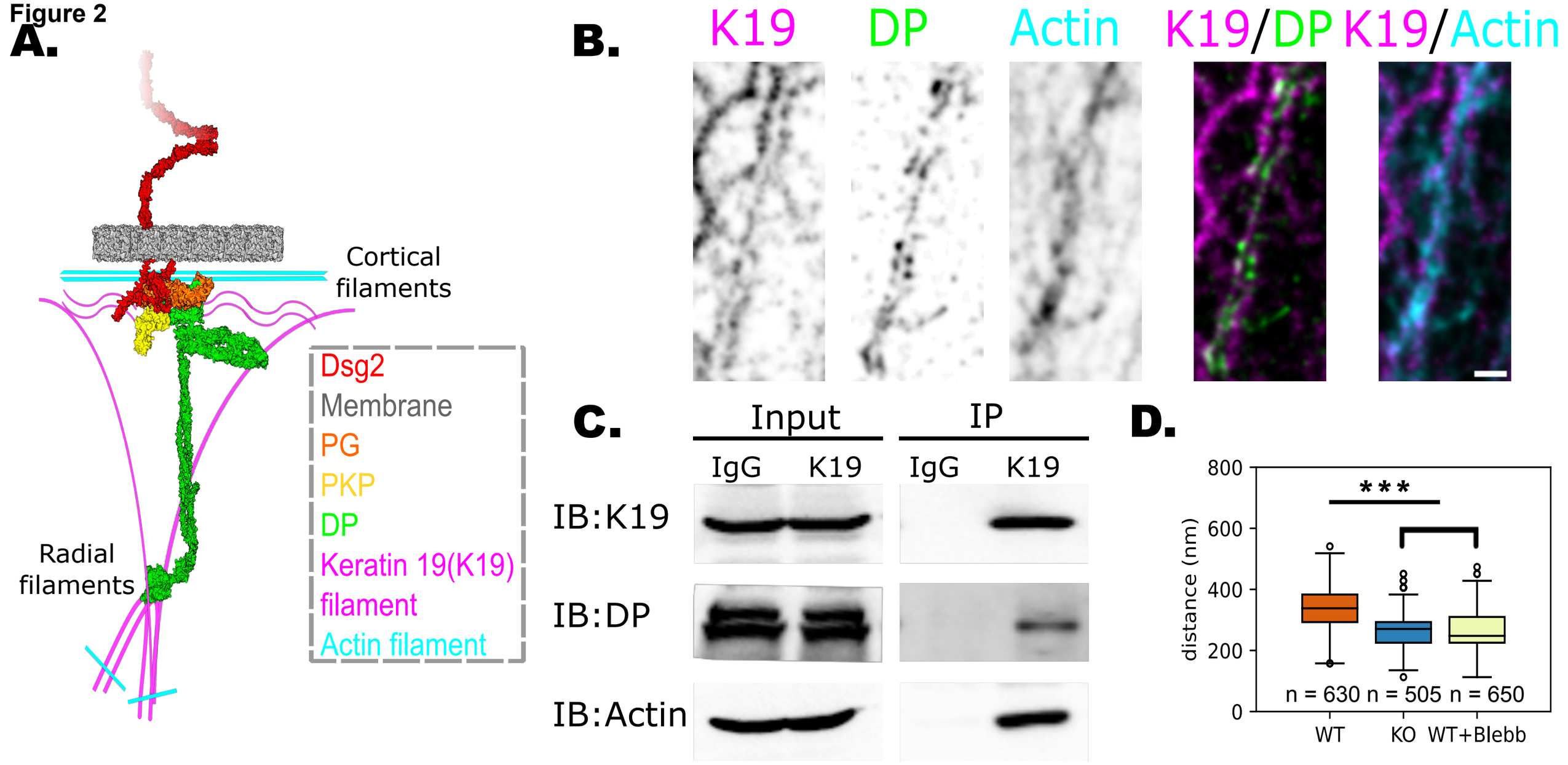
A.
Cortical filaments
Radial filaments
Dsg2
Membrane
PG
PKP
DP
Keratin 19(K19) filament
Actin filament
B.
K19
DP
Actin
K19/DP
K19/Actin
C.
Input
IP
IgG
K19
IgG
K19
IB:K19
IB:DP
IB:Actin
D.
800
600
400
200
0
distance (nm)
***
n = 630
n = 505
n = 650
WT
KO
WT+Blebb

Figure 3 Dsg2 Extracellular Region

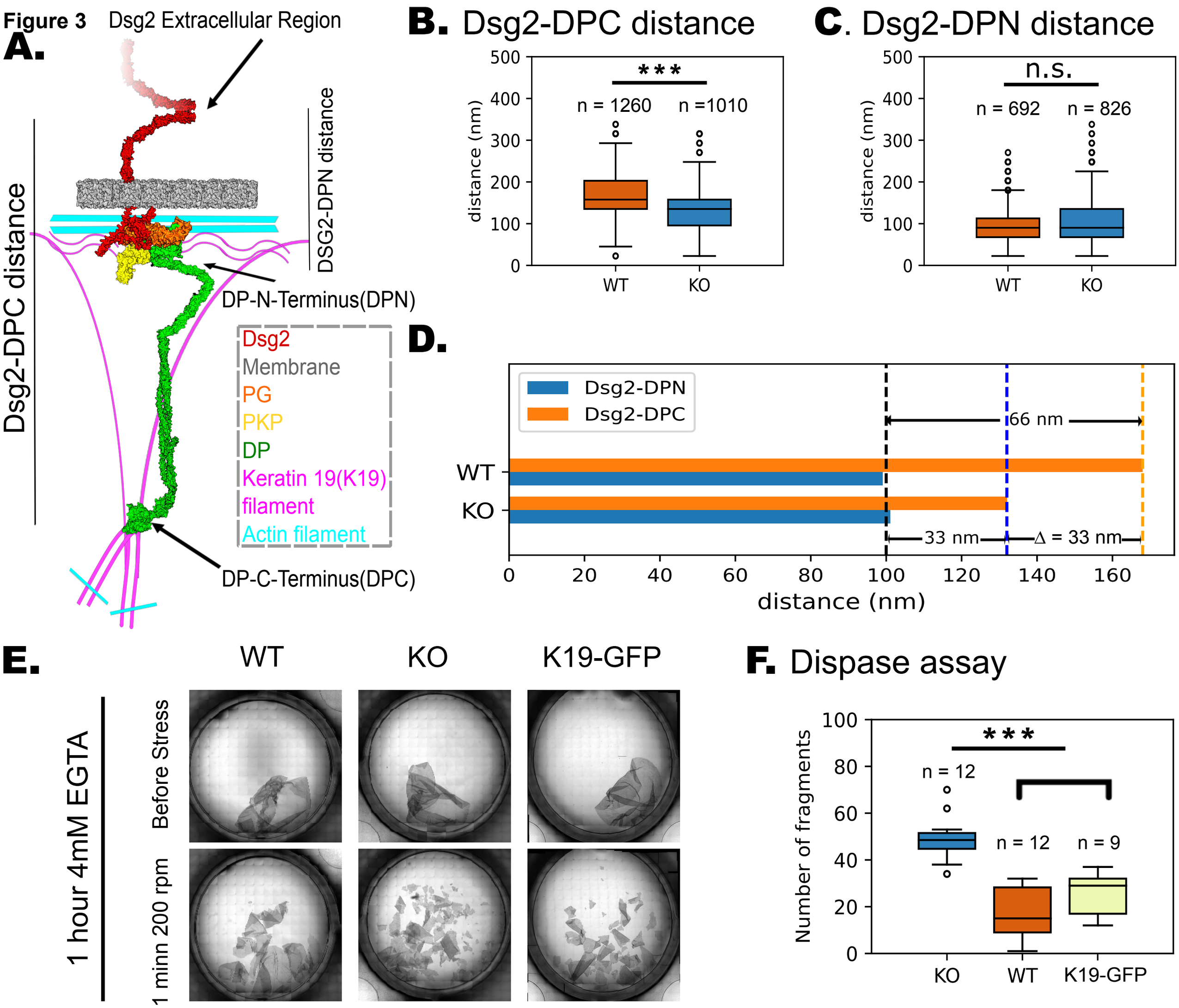

Figure 4

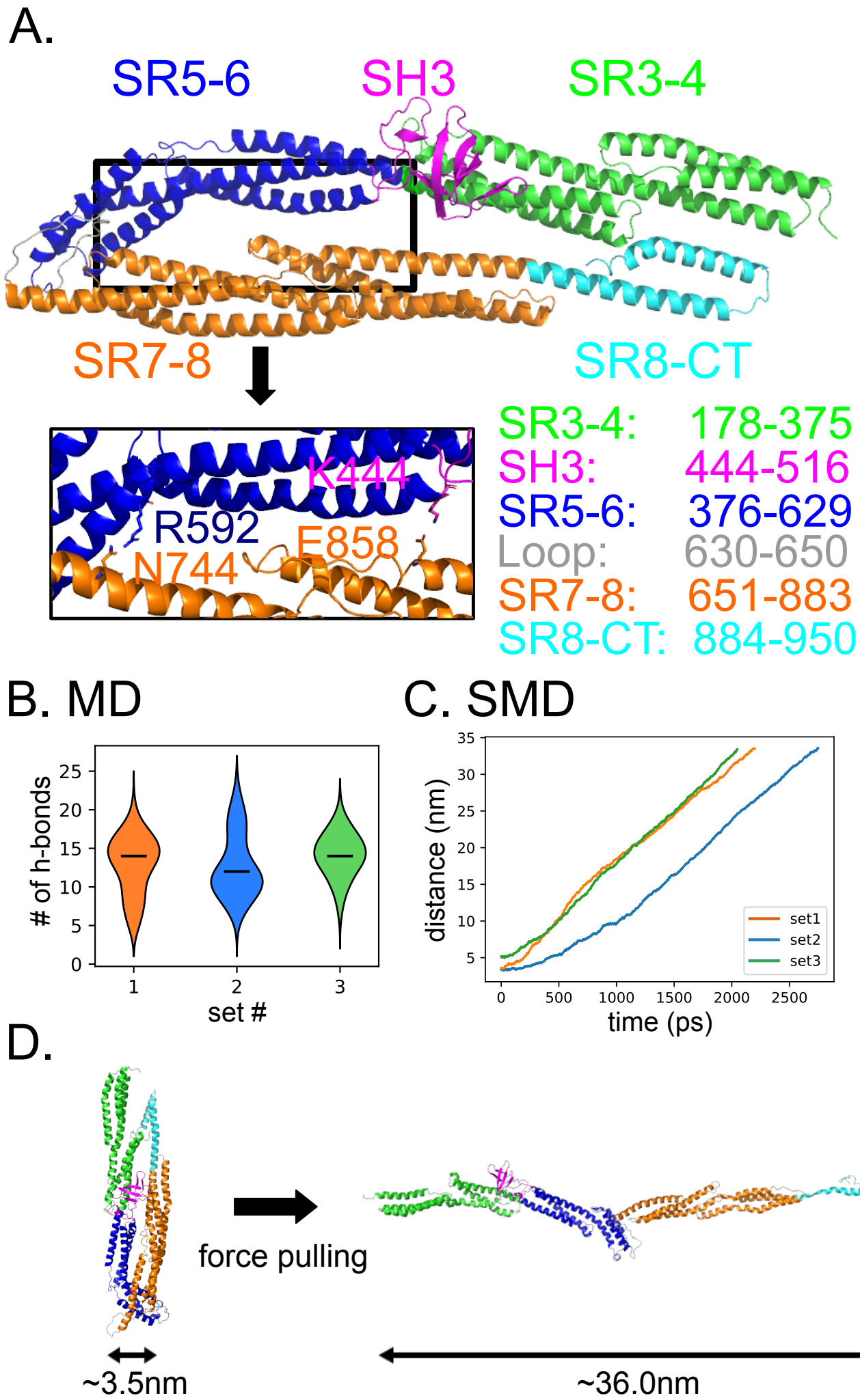
A.
SR5-6
SH3
SR3-4
SR7-8
SR8-CT
K444
R592
E858
N744
SR3-4: 178-375
SH3: 444-516
SR5-6: 376-629
Loop: 630-650
SR7-8: 651-883
SR8-CT: 884-950
B. MD
# of h-bonds
set #
C. SMD
distance (nm)
time (ps)
set1
set2
set3
D.
force pulling
~3.5nm
~36.0nm